

# Time-Resolved Luminescence Nanothermometry with Nitrogen-Vacancy Centers in Nanodiamonds

Yan-Kai Tzeng,<sup>†,‡,⊥</sup> Pei-Chang Tsai,<sup>†,⊥</sup> Hsiou-Yuan Liu,<sup>†,§</sup> Oliver Y. Chen,<sup>†</sup> Hsiang Hsu,<sup>†</sup> Fu-Goul Yee,<sup>§</sup> Ming-Shien Chang,<sup>\*,†</sup> and Huan-Cheng Chang<sup>\*,†,||</sup>

<sup>†</sup>Institute of Atomic and Molecular Sciences, Academia Sinica, Taipei 106, Taiwan

<sup>‡</sup>Department of Chemistry, National Taiwan University, Taipei 106, Taiwan

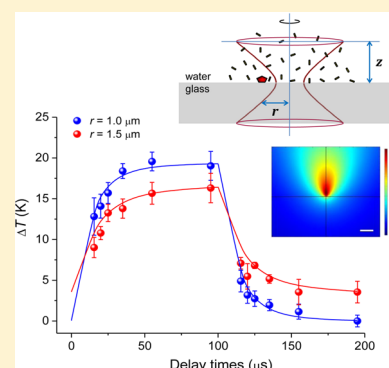
<sup>§</sup>Department of Physics, National Taiwan University, Taipei 106, Taiwan

<sup>||</sup>Department of Chemical Engineering, National Taiwan University of Science and Technology, Taipei 106, Taiwan

## Supporting Information

**ABSTRACT:** Measuring temperature in nanoscale spatial resolution either at or far from equilibrium is of importance in many scientific and technological applications. Although negatively charged nitrogen-vacancy (NV<sup>−</sup>) centers in diamond have recently emerged as a promising nanometric temperature sensor, the technique has been applied only under steady state conditions so far. Here, we present a three-point sampling method that allows real-time monitoring of the temperature changes over  $\pm 100$  K and a pump–probe-type experiment that enables the study of nanoscale heat transfer with a temporal resolution of better than  $10\ \mu\text{s}$ . The utility of the time-resolved luminescence nanothermometry was demonstrated with  $100\ \text{nm}$  fluorescent nanodiamonds spin-coated on a glass substrate and submerged in gold nanorod solution heated by a near-infrared laser, and the validity of the measurements was verified with finite-element numerical simulations. The combined theoretical and experimental approaches will be useful to implement time-resolved temperature sensing in laser processing of materials and even for devices in operation at the nanometer scale.

**KEYWORDS:** color center, diamond nanoparticle, electron spin resonance, gold nanorod, single particle tracking, time-resolved thermometry



The measurement of temperature with nanoscale spatial resolution is an emerging new technology in recent years,<sup>1,2</sup> and the development of this so-called nanothermometry is expected to have important impacts in various fields of science and technology. An ideal nanothermometer should be not only accurate but also applicable over a wide temperature range and under diverse environmental conditions, and the measurement time should be short enough to allow following the time evolution of the system under interrogation. A number of luminescence-based nanothermometers have been developed in the past using nanosized particles such as semiconductor quantum dots, rare earth doped oxides, luminescent nanogels, and so forth.<sup>1,2</sup> Gold nanoparticles<sup>3</sup> and fluorescent nanodiamonds (FNDs)<sup>4–7</sup> are new additions to the application. Of particular interest is the FND, which contains negatively charged nitrogen-vacancy (NV<sup>−</sup>) color centers as built-in fluorophores. The center has recently been demonstrated to play a significant role in several core branches of science such as quantum optics, spintronics, magnetic sensing, and bioimaging.<sup>8–10</sup> The ground state of NV<sup>−</sup> is a spin triplet formed by two unpaired electrons with a crystal field splitting of  $2.87\ \text{GHz}$  separating  $m_s = 0$  and  $m_s = \pm 1$  sublevels. Interestingly, the spin states of NV<sup>−</sup> can be optically polarized and coherently manipulated by microwave radiation, a technique known as

optically detected magnetic resonance (ODMR), even at the single molecule level.<sup>11,12</sup> As the spin properties of NV<sup>−</sup> are sensitive to environmental temperature changes,<sup>4–7,13–15</sup> the FND can serve as a quantum thermometer. This unique property, together with its chemical inertness, mechanical robustness, excellent photostability, and inherent biocompatibility, makes FND appealing for a wide range of applications.<sup>16,17</sup>

A typical method to realize the NV-based nanothermometry is to measure the thermal shifts of the ODMR peaks. However, it is time-consuming to acquire the whole ODMR spectrum and postdata processing is required to determine the peak position. Although coherent control methods have made it possible to conduct temperature measurement with ultrahigh precision at thermal equilibrium,<sup>5,6,13</sup> applications of the techniques to real-time temperature monitoring or mapping of the temporal temperature profile of a system far from equilibrium are still a challenge. Here, we present a three-point sampling method that not only allows determination of the temperature change by more than  $100\ \text{K}$  on the fly but also is

**Received:** March 2, 2015

**Revised:** April 19, 2015

**Published:** May 7, 2015

able to stroboscopically probe the temporal evolution of temperature down to 10  $\mu$ s resolution. The method is based on two previous observations for bulk diamond that the widths (typically 10 MHz) of the ODMR peaks only vary by less than 10%, whereas their peak positions are shifted by more than 20 MHz over 300–700 K.<sup>14,15</sup> Assuming a constant width, one can determine the temperature shift by measuring the changes of the fluorescence dip at three preselected frequencies without scanning the whole ODMR spectrum. This enables real-time measurement of the temperature changes over  $\pm 100$  K with respect to a known initial temperature and, more importantly, the study of nanoscale heat transfer dynamics in a pump–probe configuration with a pulsed heating source.

In applying NV<sup>−</sup> centers for time-resolved luminescence nanothermometry, we chose to use FNDs of  $\sim 100$  nm in diameter as the temperature sensor and gold nanorods (GNRs) with a diameter of 10 nm and a length of 41 nm as the photon energy absorber. The FND prepared for this work has a NV<sup>−</sup> density close to 10 ppm, or  $\sim 900$  NV<sup>−</sup> centers per 100 nm particle.<sup>18</sup> The GNR, on the other hand, has an intense longitudinal surface plasmon resonance (SPR) band peaking at  $\sim 800$  nm,<sup>19</sup> which is well separate from both the excitation wavelength (500–600 nm) and emission wavelength (650–800 nm) of the NV<sup>−</sup> centers.<sup>20</sup> We first employed near-infrared light to achieve highly localized heating of the GNRs in aqueous solution and then applied the three-point method to monitor local temperature changes with single FNDs. Pump–probe-type experiments were subsequently carried out to determine the nanoscale heat transfer rates using microsecond laser pulses. Results of the measurements were finally compared with finite-element numerical simulations.

**Results and Discussion.** The experimental setup comprised a confocal fluorescence microscope coupled with two microwave sources and two continuous-wave (CW) lasers operating at the green (532 nm) and near-infrared (808 nm) regions for the excitation of FND and GNR, respectively (Figure 1a). A thin gold wire delivered the microwaves to the FND samples spin-coated on a glass coverslip to induce the transitions between the  $m_s = 0$  and  $m_s = \pm 1$  sublevels of NV<sup>−</sup> centers.<sup>21,22</sup> To avoid detachment of the particles from the coverslip when the local temperature was largely changed by laser heating, the FNDs were covalently coated with cationic polymers such as polyarginine,<sup>23</sup> and so they could be firmly anchored to the negatively charged glass surface through electrostatic attraction. Additionally, to ensure long-term observation of the same particles under investigation, which is imperative to the present measurement, a three-dimensional (3D) confocal fluorescence tracking technique has been implemented.<sup>24</sup> This was achieved by feedback controlling a three-axis piezo-scanning stage on which a 100 $\times$  microscope objective was mounted, with a user-developed program to maintain constant fluorescence intensities at the center ( $x = y = 0$ ) as well as four selected points ( $x = \pm 50$  nm and  $y = \pm 50$  nm) in the point spread function of the fluorescence spots (Figure 1b). Real-time tracking of the movement of an interrogated FND can be made indefinitely, as long as it moves less than the maximum tracking speed (450 nm/s) and stays within our capture range of  $30 \times 30 \times 10 \mu\text{m}^3$  in  $x$ ,  $y$ , and  $z$  directions (Figure 1c).

Figure 2 displays typical ODMR spectra taken with a data acquisition time of  $\sim 3$  min for a single 100 nm FND particle on a glass coverslip. Both the microwave and the 532 nm probe laser were run in CW mode, and the resultant fluorescence

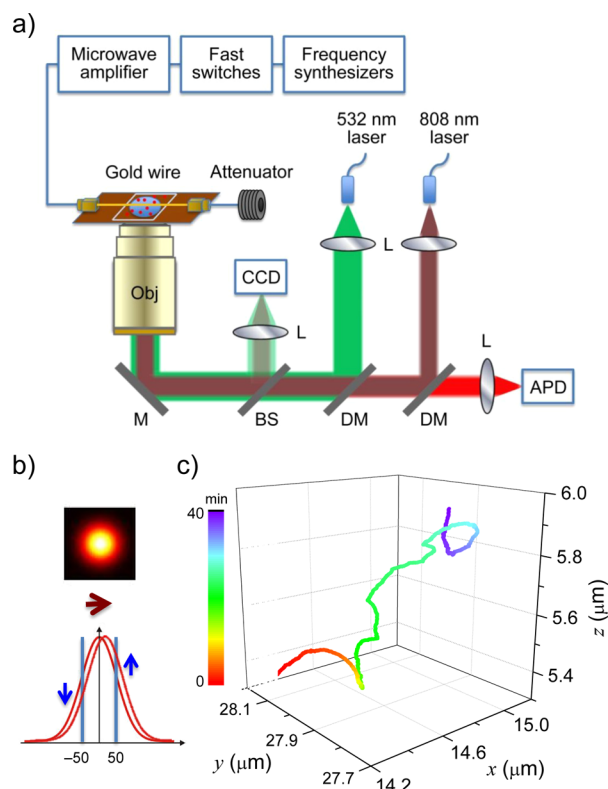


**Figure 1.** Experimental setup and single particle tracking. (a) Schematic diagram of the experimental setup. APD, avalanche photodiode; BS, beam splitter; DM, dichroic mirror; CCD, charge-coupled device; L, lens; M, mirror; and Obj, objective. Red dots on the glass coverslip denote FNDs. (b) Fluorescence image of a single FND particle spin-coated on a glass coverslip, acquired by confocal microscopy. The profile is well described by a Gaussian point spread function. Changes in the fluorescence intensity at the peak center ( $x = y = 0$ ) and at  $\pm 50$  nm from the center in both  $x$  and  $y$  directions are analyzed with a computer program and used to determine the position of the particle in three dimensions. (c) Three-dimensional tracking of a single FND particle over a time period of 40 min.

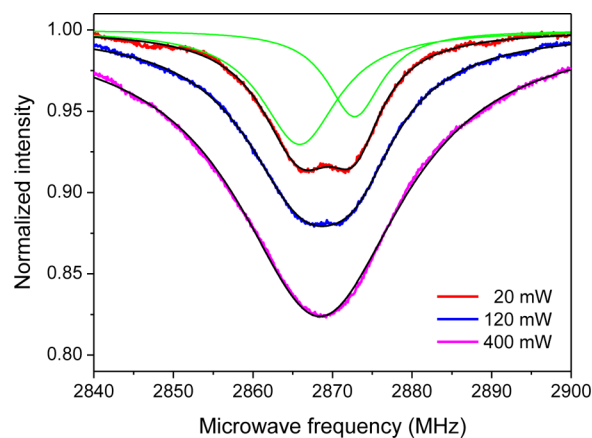


**Figure 2.** Spin transition. ODMR spectra of a 100 nm FND spin-coated on a glass substrate, obtained with three different microwave powers (20, 120, and 400 mW). All the spectra can be well fitted with either one or two Lorentzian functions (black and green curves).

photons were detected at each microwave frequency by an avalanche photodiode. At room temperature, a dip with a depth of  $\sim 9\%$  was found at  $\omega_0 = 2868.4 \pm 0.1$  MHz. It split into two

components ( $\Delta m_s = \pm 1$ ) due to the presence of localized crystallographic strain and they could be well fitted by two Lorentzian functions. The dips were significantly broadened as the microwave power was increased from 20 to 400 mW, at which the spectrum exhibited a single Lorentzian-like profile with a depth of  $\sim 18\%$  and an effective width of  $\gamma = 12.7$  MHz. Taking the thermal shift of the ODMR peak as  $\Delta D/\Delta T = -0.075$  MHz/K,<sup>14</sup> the error involved in the curve fitting to find  $\omega_0$  corresponds to a temperature measurement uncertainty of  $\sim 1$  K.

**Three Point Method.** To expedite the thermometric analysis, we measured the fluorescence intensities at three frequencies only, where  $f_1$  and  $f_2$  are the frequencies at the half depth of the dip at a known temperature, and  $f_3$  is a far-off resonant frequency at which the microwave has no observable effect on the ground state spins of the NV<sup>-</sup> center. Two assumptions are made in this three-point method: (1) an ODMR spectrum is effectively composed of either one or two Lorentzian peaks and (2) the widths of the peaks are insensitive to temperature changes. To simplify the analysis, we first consider an ODMR spectrum consisting of only one Lorentzian peak with a constant width  $2\gamma$ , thus  $f_1 = \omega_0 - \gamma$  and  $f_2 = \omega_0 + \gamma$  (Figure 3a). Starting with the Lorentzian function

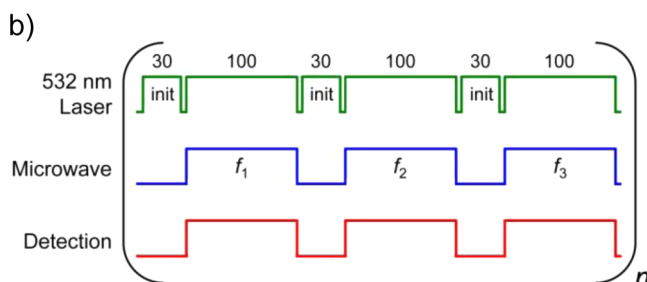
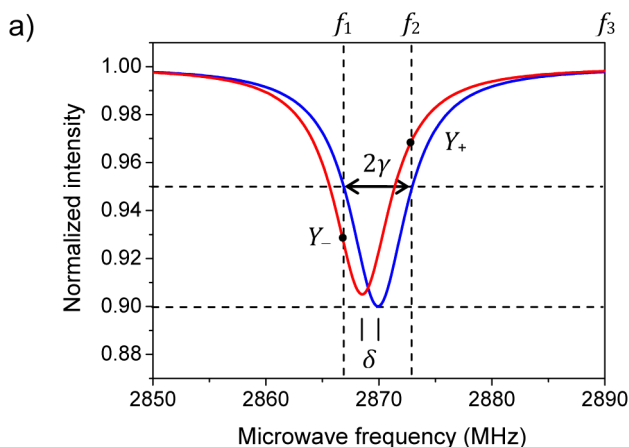


**Figure 3.** Three point method. (a) Pictorial presentation of the three-point method based on an ODMR spectrum consisting of only one peak. The peaks before (blue) and after (red) temperature change are both Lorentzian and have the same width, although their heights may differ. Overlaid on the spectra are three frequencies ( $f_1, f_2, f_3$ ) chosen for the intensity measurement and  $Y_{\pm}$  denote the points where the normalized sampled heights were measured. (b) Timing sequences of the laser irradiation, microwave excitation, and fluorescence detection in the three-point method. The separations between initiation (init) and detection pulses are all 1  $\mu$ s. The typical number of cycles was  $n = 70\,000$  in this experiment.

$$\mathcal{L}(\omega) = \frac{A\gamma}{(\omega - \omega_0)^2 + \gamma^2} \quad (1)$$

where  $A/\gamma$  is the peak height, theoretical treatments as detailed in Supporting Information show that the temperature-dependent peak shift ( $\delta$ ) can be calculated by

$$\delta = \gamma \cdot \frac{1 \pm \sqrt{1 - 2R^2}}{R} \quad (2)$$

where

$$R = \frac{Y_+ - Y_-}{Y_+ + Y_-} \quad (3)$$

Here, the normalized sampled heights  $Y_{\pm}$  are defined as

$$Y_+ = \frac{I_3 - I_2}{I_3 - I_0} \quad (4)$$

$$Y_- = \frac{I_3 - I_1}{I_3 - I_0} \quad (5)$$

where  $I_1, I_2$ , and  $I_3$  are the fluorescence intensities measured at points  $f_1, f_2$ , and  $f_3$ , respectively, and  $I_0$  is the fluorescence intensity at the center frequency of the shifted peak (Figure 3a). Experimentally,  $I_0$  cannot be known without scanning the whole ODMR spectrum; however, the ratio  $R$  can be determined without knowing it as

$$R = -\frac{I_2 - I_1}{2I_3 - I_2 - I_1} \quad (6)$$

Under the condition that  $|\delta| \leq (2)^{1/2}\gamma$ , the solution in eq 2 takes a negative sign. Given  $\gamma = 12.7$  MHz as shown in Figure 2, a working range of up to  $\Delta T = \pm 160$  K can be inferred from the thermal shift measurements of Toyli et al.<sup>15</sup> and Plakhotnik et al.<sup>7</sup> At  $|\delta| \ll \gamma$ , eq 2 can be approximated by

$$\delta = -\gamma \cdot \frac{I_2 - I_1}{2I_3 - I_2 - I_1} \quad (7)$$

In cases where the ODMR spectrum cannot be fitted with a single Lorentzian function and the simple model introduced above is invalid, one can generalize the above analysis to treat more complicated cases (See Supporting Information and Figure S1 and S2 for further details). Alternatively, the spectral shift can be deduced by finding numerically the inversion of  $R(\delta)$ , that is,  $\delta(R)$ , based on the measured intensities and the prescanned ODMR spectra (Supporting Information Figure S3).

An advantage of this three-point method is that it possesses a built-in ability for self-correction of signal fluctuation. Shot-to-shot fluorescence intensity fluctuations and background noises can be effectively eliminated because they are common in both the numerator and denominator terms of eq 6. Experimentally, the three-point method is easily implemented by using two microwave synthesizers whose output frequencies ( $f_1$  and  $f_2$ ) are preselected according to the prescanned ODMR spectra. Fluorescence signals of the third frequency ( $f_3$ ) are then collected when both the microwave sources are switched off. Figure 3b illustrates the pulse sequences of the laser excitation, microwave excitation, and photon detection at the three frequencies. The measurement rejects low-frequency fluctuations up to 2.5 kHz, as each cycle took only  $\sim 400$   $\mu$ s. Given a photon count rate of  $1 \times 10^6$  counts/s at each probed



frequency, the shot-noise-limited sensitivity of this method was estimated to be  $\sim 2 \text{ K}/(\text{Hz})^{1/2}$ , which could be readily achieved in experiments (Supporting Information Figure S4). Further improvement of the sensitivity is possible by increasing the photon counting rate, together with the use of a better microwave antenna such as a lithographic antenna that will yield more stable and deeper ODMR dips.

We may compare the present approach with a previous method developed by Kucsko et al.<sup>5</sup> who sampled four points of the ODMR spectrum to extract the thermal shift. Assuming a linear response of the fluorescence intensity in ODMR to temperature, they achieved a temperature measurement precision of  $\sim 0.1 \text{ K}$  in 4 s using a high photon counting rate and a coplanar waveguide for microwave excitation. However, the working range of the method is limited to about  $\pm 15 \text{ K}$  (or  $\pm 1 \text{ MHz}$  in thermal shift) due to the linear temperature dependence assumption. In comparison, our method is about  $3\times$  lower in sensitivity but has a much wider ( $\sim 10\times$ ) working range, and the analytical relationship between the frequency shift and the measured fluorescence intensities is available even at large temperature changes, that is, eq 2. Moreover, the method is extendable to time-domain measurement by performing pump–probe-type experiments using a pulsed laser as the heating source.

**Temporally and Spatially Resolved Nanothermometry.** As a proof-of-principle experiment, we first employed the FNDs to measure the nanoscale temperature of a system at the steady state. We spin-coated the NV-based temperature sensors on a glass coverslip and submerged them in GNR solution within a microchannel ( $\sim 1 \text{ mm}$  height,  $\sim 2 \text{ mm}$  width, and  $\sim 8 \text{ mm}$  length). Selecting a single FND particle in the channel, we acquired its ODMR spectra in the solution with a total volume of  $\sim 20 \mu\text{L}$  and an optical density (OD) of  $\sim 10$ . A drastic change of the solution temperature from 298 to 405 K was recorded as the GNRs were heated by the CW near-infrared (NIR) laser with its power increasing from  $P_{\text{NIR}} = 0$  to 10 mW (Figure 4a). These temperatures were deduced based on the calibration curve provided by Toyli et al.<sup>15</sup> over 300–700 K. It is noted that the highest temperature (405 K) measured in this experiment substantially exceeds 373 K, that is, the normal boiling point of water, implying that superheating of the GNR solution has occurred.<sup>25,26</sup> Thanks to the poor spectral overlap between these two nanomaterials (Supporting Information Figure S5), no noticeable quenching of the FND fluorescence by GNRs was observed. Furthermore, the effect of heating the GNR solution by the green laser alone (power less than  $10 \mu\text{W}$ ) was negligible.

We next characterized the time-dependent temperature response of the GNR solution using the three-point method and a mechanical shutter to control the on/off status of the 808 nm laser. With  $P_{\text{NIR}} = 7.8 \text{ mW}$ , a quick rise of the solution temperature by  $\sim 90 \text{ K}$  in 30 s was achieved and it rapidly dropped back to room temperature within the same time interval when the laser was turned off (Figure 4b). In contrast, it took about 10 min for the temperature of the GNR solution (OD  $\sim 1$ ) of 1 mL volume to reach its steady state value ( $\Delta T \sim 40 \text{ K}$  at  $P_{\text{NIR}} = 0.6 \text{ W}$ ) using the same laser without focusing (Figure 4c).<sup>27</sup> It is noteworthy in Figure 4a that the widths of the ODMR peaks stay nearly the same over the temperature variation range of 298–405 K, strongly supporting the basic assumption of the three-point method.

The availability of the three-point method allowed us to measure the nanoscale heat transfer rates by performing

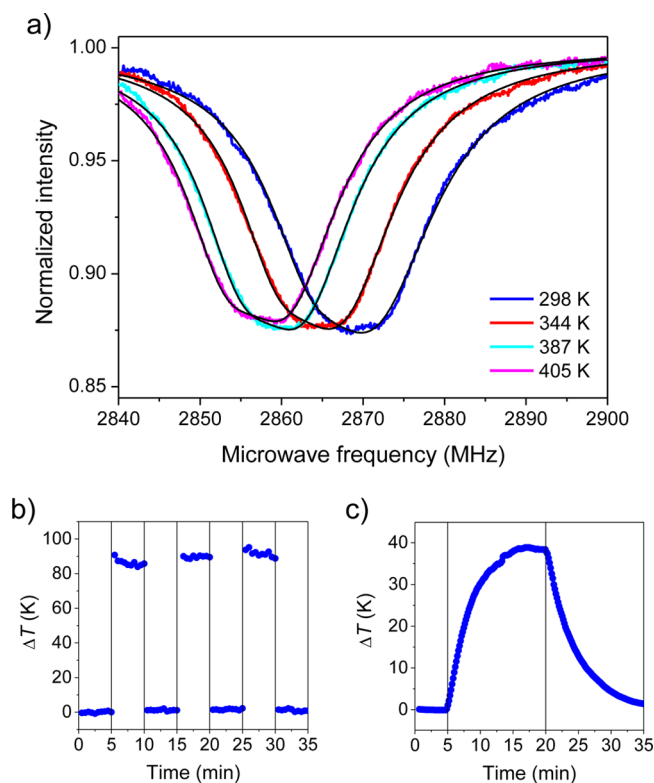


**Figure 4.** Superheating water. (a) ODMR spectra of an FND particle submerged in aqueous solution containing  $10 \text{ nm} \times 41 \text{ nm}$  GNR heated by an 808 nm laser with its power varying from 0 to 10 mW. (b) Modulation of the temperature of the GNR solution ( $20 \mu\text{L}$  and OD  $\sim 10$  at 808 nm) in a microchannel by turning the laser ( $P_{\text{NIR}} = 7.8 \text{ mW}$ ) on and off every 5 min. (c) Photothermal measurement of the GNR solution (1 mL and OD  $\sim 1$  at 808 nm) in a cuvette. The 808 nm excitation laser with an output power of 0.6 W was turned on for 15 min and then off to reveal the energy absorption and heat dissipation processes.

pump–probe-type experiments. First, to ensure good spatial overlap between the pump (808 nm) and probe (532 nm) lasers, the lateral and axial point spread functions (PSFs) of these two laser beams at the foci (i.e.,  $r = z = 0$  as indicated in Figure 5a) were closely examined by collecting their respective scattered light from a gold nanoparticle of 80 nm in diameter.<sup>28</sup> Second, the heating laser was switched on and off using an acousto-optic modulator with a response time of 5 ns. Third, the widths of both the initiation and detection laser pulses were reduced to  $10 \mu\text{s}$  (Figure 5b) in order to achieve the highest possible temporal resolution at the expense of sensitivity. Fourth, the FNDs were covalently conjugated with cationic polymers (such as polyarginine<sup>23</sup>) to prevent attachment of the positively charged GNRs to their surfaces. Finally, the focus of the 808 nm laser beam was intentionally separated from the FND by a distance ( $r$ ) of more than  $1 \mu\text{m}$  to avoid direct heating of the temperature sensor and reduction of the ODMR dip depth due to the NIR excitation.<sup>29</sup>

Figure 5c shows results of the temperature measurement as a function of the delays between pump and probe laser pulses at  $P_{\text{NIR}} = 3.9 \text{ mW}$  and  $r = 1.0$  and  $1.5 \mu\text{m}$ . By fitting the experimental data to the exponential recovery function  $\Delta T = A + B[1 - \exp(-t/\tau)]$  for the temperature rising and the exponential decay function  $\Delta T = A + B\exp(-t/\tau)$  for the temperature falling, we determined a time constant of  $\tau = 12 \pm 1 \mu\text{s}$  at  $r = 1.0 \mu\text{m}$  and  $\tau = 18 \pm 3 \mu\text{s}$  at  $r = 1.5 \mu\text{m}$  for the

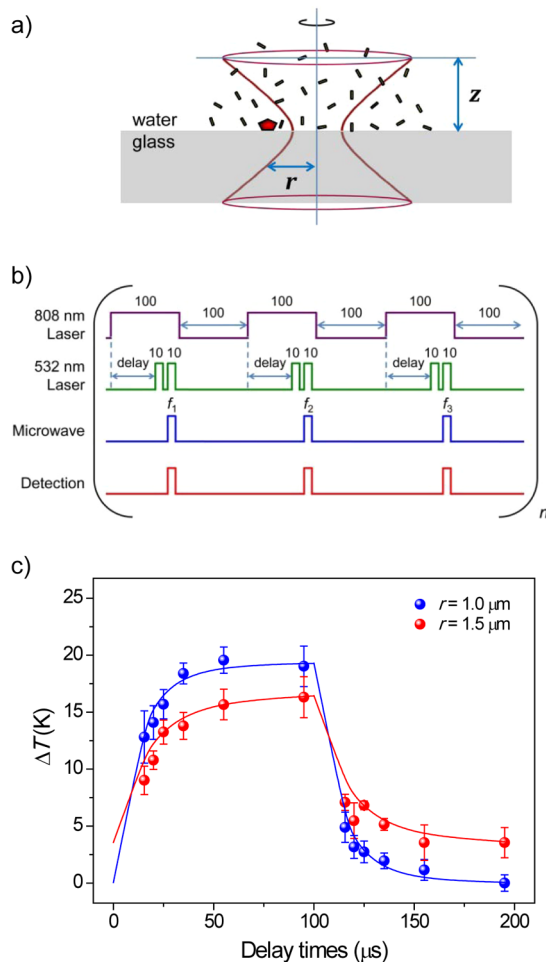


**Figure 5.** Temporally and spatially resolved nanothermometry. (a) Pictorial presentation of the experiment using an 808 nm laser for the heating of GNRs in water and a single FND particle for temperature sensing. The separation between FND and the 808 nm laser beam focus is denoted as  $r$  and the distance from the water–glass interface (and the 808 nm laser beam waist) to the point of interest is denoted as  $z$ . (b) Timing sequences of the 532 and 808 nm laser irradiation, microwave excitation, and fluorescence detection for time-resolved temperature measurement. All numbers are in units of microseconds and both the microwave and detection pulses are in synchronization with the 532 nm laser pulses. (c) Time evolution of the heat dissipation for a GNR solution irradiated with a pulsed 808 nm laser ( $P_{\text{NIR}} = 3.9$  mW) at  $z \sim 0$   $\mu\text{m}$  and  $r = 1.0$  and  $1.5$   $\mu\text{m}$ . Solid curves are best fits of the experimental data to exponential recovery and decay curves with the same time constants, amplitudes, and offsets.

heating with a pulse duration of 100  $\mu\text{s}$  and an interpulse interval of 200  $\mu\text{s}$  (Figure 5b). Note that these two measured time constants should not be associated with the rate of the energy loss of the heated GNR particle to its environment (i.e., water and the glass substrate), because the process has been predicted to occur within 1 ns due to phonon–phonon coupling.<sup>30,31</sup> They should instead represent the time required for the heat to dissipate out of the laser excitation region,<sup>32</sup> of which the measured local transient temperatures can be properly defined in the microsecond time scale.

**Numerical Simulations.** To verify the validity of the time-resolved temperature measurements and to understand the heat transfer in the nanometer and microsecond scales, we carried out numerical simulations. Our theoretical modeling was based on the assumptions that (1) the attenuation of the laser beam

can be properly described by an effective absorption coefficient  $\alpha$  of the GNR solution, (2) the energy absorbed by the GNRs are totally released as heat to water within our probing time of 10  $\mu\text{s}$ , and (3) melting and thus reshaping<sup>33,34</sup> of GNRs do not occur during the course of the measurements. For simplicity, the model took only the laser-induced heat source and the conduction dissipation into consideration. We solved the heat conduction equation by finite element analysis with the COMSOL program (Multiphysics) for a uniform medium heated by a focused Gaussian laser beam in the cylindrical coordinate at  $z \geq 0$  as<sup>35,36</sup>

$$\frac{\rho C_p}{k} \frac{\partial T}{\partial t} = \frac{\partial^2 T(r, z, t)}{\partial r^2} + \frac{1}{r} \frac{\partial T(r, z, t)}{\partial r} + \frac{\partial^2 T(r, z, t)}{\partial z^2} + \frac{\alpha I(r, z, t)}{k} \quad (8)$$

where the laser intensity profile was approximated by

$$I(r, z, t) = I_0(t) \left( \frac{w_0}{w(z)} \right)^2 \exp \left[ -2 \left( \frac{r}{w(z)} \right)^2 - \alpha z \right] \quad (9)$$

with

$$w(z) = w_0 \sqrt{1 + \left( \frac{\lambda z}{\pi w_0^2 n} \right)^2} \quad (10)$$

in which  $r$  and  $z$  are the radial and axial coordinates,  $\rho$ ,  $C_p$ ,  $k$ , and  $n$  are the density, specific heat capacity, thermal conductivity, and refractive index of the liquid, respectively,  $w_0$  is the Gaussian beam waist,  $\lambda$  is the wavelength of the heating laser, and  $I_0(t)$  is the intensity at the center of the laser beam at its waist and is related to its total power by  $P_0(t) = \pi w_0^2 I_0(t)/2$ . At the water–glass interface, the following two boundary conditions apply<sup>36</sup>

$$T(r, z = 0, t) = T_s(r, z = 0, t) \quad (11)$$

$$k \left( \frac{\partial T}{\partial z} \right)_{r, z=0, t} = k_s \left( \frac{\partial T_s}{\partial z} \right)_{r, z=0, t} \quad (12)$$

where the subscript “s” denotes the substrate. Given the values of the parameters  $\rho C_p = 4.18$  J/cm<sup>3</sup>·K,  $k = 0.58$  W/m·K, and  $n = 1.33$  for water,  $k_s = 1.3$  W/m·K for the coverslip glass,  $\alpha \sim 230$  cm<sup>−1</sup> for the GNR solution, and  $\lambda = 808$  nm,  $w_0 \sim 0.23$   $\mu\text{m}$ ,  $P_0(t) = 0$  or 3.9 mW (depending on the laser on or off) for the heating laser, we obtained the temporal profiles of the GNR solution from the numerical simulations under the boundary conditions of  $\Delta T = 0$  K at  $z = -0.5$  and 1.0 mm and  $r = 3.0$  mm. The simulated time constants for single exponential decays are  $\tau = 20$   $\mu\text{s}$  at  $r = 1.0$   $\mu\text{m}$  and  $\tau = 25$   $\mu\text{s}$  at  $r = 1.5$   $\mu\text{m}$  (Figure 6a), compared with our experimental observations of 12 and 18  $\mu\text{s}$ , respectively. The agreement between simulation and experiment is satisfactory, considering that the probing laser pulses are 10  $\mu\text{s}$  in width and the intensity distribution of the heating laser beam is highly heterogeneous due to the tight focusing. The overall differences between the simulated and measured results in  $\Delta T$  are within  $\pm 2$  K without any free parameter adjustment in the simulations (Figure 6b).

In Figure 6a, we also show how the solution temperature varies with the distance of  $r = 0$ –3  $\mu\text{m}$  at  $z = 0$   $\mu\text{m}$  when the number of the heating laser pulses increases (up to 30), as predicted by the theoretical simulations. The prediction of a

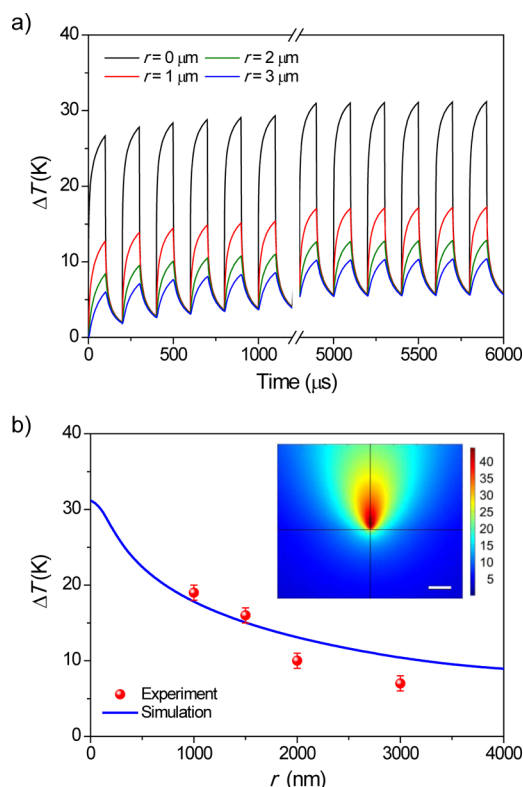


**Figure 6.** Numerical simulations. (a) Temporal and spatial profiles of the laser-heated GNR solution, simulated by solving the heat conduction equations described in text and COMSOL. (b) Comparison of the measured and simulated spatial dependences of the temperature rises at  $z = 0$  as a function of  $r$  at the steady state (i.e., at 5900  $\mu$ s). Inset: Two-dimensional temperature profile in the  $r$ - $z$  plane near the laser heating region. Scale bar is  $2 \mu\text{m}$ .

decrease in the amplitude of the temperature modulation as  $r$  increases is in line with our experimental observations. At  $r = 0 \mu\text{m}$ , the temperature decay clearly consists of two components, fast ( $\tau_1 = 1.2 \mu\text{s}$ ) and slow ( $\tau_2 = 25.8 \mu\text{s}$ ), with an amplitude ratio of 3:2. The former is contributed by the rapid laser heating and subsequent energy loss in the excitation region, whereas the latter is due to the slower rate of the heat dissipation out of the laser focal volume. At  $r > 3 \mu\text{m}$ , the amplitude of the fast component is too small to be seen (data not shown). Figure 6b illustrates the  $r$  dependence of the temperature rise at  $z = 0$  and the steady state (i.e., at 5900  $\mu$ s). The corresponding temperature profile in the  $r$ - $z$  plane is shown in the inset. As noted, the temperature distribution in  $r$  can be better represented by error functions<sup>35</sup> than reciprocal functions for a point thermal source. The hottest spot in this laser-heated region is at  $z = 0 \mu\text{m}$  and  $r = 0.50 \mu\text{m}$  with a temperature rise as high as 44 K (Supporting Information Figure S6). Superheating of the aqueous solution near the water-glass interface can thus be established when the laser power is increased to  $P_{\text{NIR}} = 7.8 \text{ mW}$  or higher, as illustrated in Figure 4a.

It is instructive to compare this work with two previous studies on similar topics. Richardson et al.<sup>32</sup> performed a set of experiments on photoheating of 20 nm gold nanoparticles in a water droplet ( $\sim 2 \text{ mm}$  in diameter) with a CW 532 nm laser, a mechanical chopper, and a thermocouple for temperature measurement. They obtained a light-to-heat conversion efficiency of  $\sim 1$  and a heat loss time constant of  $\tau = 8.3 \text{ s}$ .

Cordero et al.<sup>36</sup> measured the time-resolved temperature rise of a thin water layer due to infrared laser excitation (wavelength of 1480 nm) using rhodamine B as the thermometer. The laser had a beam waist of  $5.3 \mu\text{m}$  at the focus and passed through the sample with a thickness of 1 mm. The authors achieved a spatial resolution of  $1.7 \mu\text{m}$ , as limited by the magnification of the microscope objective as well as the number of pixels on the camera sensor, and a temporal resolution of 2 ms as limited by the camera sensor's sensitivity that determined the maximum frame rate. The present experiment takes the thermometric measurements to the next level.

**Conclusion.** In this work, we have developed FND into a nanoscale luminescence thermometer for both temporally and spatially resolved temperature sensing with the hosted  $\text{NV}^-$  centers. Using microliter GNR solution as a test platform, we demonstrated the utility of a three-point method for practical temperature measurement with single FNDs submerged in the medium. A precision of better than  $\pm 1 \text{ K}$  over a temperature variation range of 100 K within a measurement time of 30 s was readily achieved. Furthermore, by employing a pulsed near-infrared laser as the heating source and the three-point method to shorten the interrogation time, a temporal resolution of better than 10  $\mu\text{s}$  has been established through pump-probe-type measurements. Such technological developments have enabled us to study highly inhomogeneous heating of water in the focal volume of a tightly focused laser beam by direct temperature measurements and to observe superheating of aqueous solution near the water-glass interface at the nanoscale. Further improvement of the technology is possible by increasing the photon counting rates and the use of a lithographic antenna for microwave excitation.<sup>5</sup> The method is expected to find practical use as a new tool to investigate nanoscale heat transfer, a process of not only fundamental interest but also technological importance.<sup>37</sup> The present study represents the first demonstration of thermometric investigation at the nanometric length scale with microsecond time resolution. It adds an important new dimension to the use of  $\text{NV}^-$  centers in diamond for quantum sensing development and applications.<sup>38,39</sup>

**Methods.** Carboxylated FNDs were produced by high-energy ion irradiation of synthetic type Ib diamond powders (Micron+, Element Six), followed by thermal annealing, air oxidation, and oxidative acid washes.<sup>18</sup> They were covalently conjugated with poly-L-arginine using water-soluble carbodiimide cross-linkers.<sup>23</sup> GNRs surface-coated with cetyltrimethylammonium bromide (CTAB) were obtained from Nanopartz and used without further modification and purification.

**Optical Setup and Temperature Measurement.** The experimental setup consisted of a modified commercial confocal microscope (IX-71, Olympus) equipped with a diode-pumped solid-state laser (DPSS, Coherent) and a Ti:sapphire laser (3900S, Newport) operating at 532 and 808 nm, respectively (Figure 1a). The 808 nm light was first reflected by a short-pass dichroic mirror (725dcspxr, Chroma) and then combined with the 532 nm light at a long-pass dichroic mirror (545dcxr, Chroma). They were focused onto the samples on a glass coverslip via a  $100\times$  oil-immersion objective (IX-71, Olympus) with a numerical aperture (NA) of 1.4, which also served to collect FND fluorescence for detection. The objective was mounted on a three-axis piezo-scanning stage (P733.3DD, Physik Instrumente), allowing for the implementation of a 3D confocal fluorescence tracking technique to achieve long-term observation of the same particle under investigation. To acquire



ODMR spectra, a thin gold wire (25  $\mu\text{m}$  in diameter) delivered the microwaves from a frequency synthesizer (PTS 3200, Programmed Test Sources) and a microwave amplifier (S183, Ophir) to excite the FNDs. The wire was situated in close proximity (within 20  $\mu\text{m}$ )<sup>22</sup> to the glass coverslip where the specimen was prepared in a microchannel constructed with two glass bars, an adhesive frame, and high vacuum silicone grease. Both the microwave and the 532 nm probe laser were run in CW mode, and the fluorescence photons ( $675 \pm 37$  nm) were detected at each scanning microwave frequency by an avalanche photodiode (SPCM-AQR-15, PerkinElmer).

Real-time monitoring of the temperature changes with the three-point method was conducted by modulating the intensities of the microwaves from two frequency synthesizers (PTS 3200, Programmed Test Sources; 12000A, Giga-tronics) with two fast switches (ZASWA-2-50DR+, Mini-Circuit) (Supporting Information Figure S7) and pulsing the lasers (532 and 808 nm) using two acousto-optic modulators (1250C, Isomet) in double-pass configuration (Supporting Information Figure S8). Two additional 808 nm laser notch filters were used to reduce the background noise level when heating the GNR sample solution with the NIR laser. The spatial separation between the heating and detection laser beams was determined based on their scattered light images with an electron multiplying charge-coupled device camera (IXON, Andor). All the laser powers reported herein were obtained after correction of the transmission of the light through the high NA objective lens in CW mode.<sup>40</sup>

## ■ ASSOCIATED CONTENT

### Supporting Information

Additional details of material preparation and characterization, particle tracking, temperature measurement utilizing ODMR, as well as the theory of the three-point method and numerical simulations of the nanoscale heat transfer. The Supporting Information is available free of charge on the ACS Publications website at DOI: 10.1021/acs.nanolett.5b00836.

## ■ AUTHOR INFORMATION

### Corresponding Authors

\*E-mail: msc@gate.sinica.edu.tw.

\*E-mail: hchang@gate.sinica.edu.tw.

### Author Contributions

<sup>†</sup>These two authors contribute equally to this work.

### Notes

The authors declare no competing financial interest.

## ■ ACKNOWLEDGMENTS

This work is supported by Academia Sinica (Grant No. AS-104-TP-A10) and the National Science Council (Grant Nos. 103-2628-M-001-005- and 100-2112-M-001-026-MY3) of Taiwan. We thank Dr. N. D. Lai for technical assistance in the early phase of this work and Prof. Y. T. Lee for kind help and generous support.

## ■ REFERENCES

- (1) Jaque, D.; Vetrone, F. Luminescence nanothermometry. *Nanoscale* **2012**, *4*, 4301–4326.
- (2) Brites, C. D. S.; Lima, P. P.; Silva, N. J. O.; Millan, A.; Amaral, V. S.; Palacio, F.; Carlos, L. D. Thermometry at the nanoscale. *Nanoscale* **2012**, *4*, 4799–4829.

- (3) Shang, L.; Stockmar, F.; Azadfar, N.; Nienhaus, G. U. Intracellular thermometry by using fluorescent gold nanoclusters. *Angew. Chem., Int. Ed.* **2013**, *52*, 11154–11157.
- (4) Plakhotnik, T.; Gruber, D. Luminescence of nitrogen-vacancy centers in nanodiamonds at temperatures between 300 and 700 K: perspectives on nanothermometry. *Phys. Chem. Chem. Phys.* **2010**, *12*, 9751–9756.
- (5) Kucsko, G.; Maurer, P. C.; Yao, N. Y.; Kubo, M.; Noh, H. J.; Lo, P. K.; Park, H.; Lukin, M. D. Nanometer-scale thermometry in a living cell. *Nature* **2013**, *500*, 54–58.
- (6) Neumann, P.; Jakobi, I.; Dolde, F.; Burk, C.; Reuter, R.; Waldherr, G.; Honert, J.; Wolf, T.; Brunner, A.; Shim, J. H.; Suter, D.; Sumiya, H.; Isoya, J.; Wrachtrup, J. High-precision nanoscale temperature sensing using single defects in diamond. *Nano Lett.* **2013**, *13*, 2738–2742.
- (7) Plakhotnik, T.; Doherty, M. W.; Cole, J. H.; Chapman, R.; Manson, N. B. All-optical thermometry and thermal properties of the optically detected spin resonances of the NV<sup>−</sup> center in nanodiamond. *Nano Lett.* **2014**, *14*, 4989–4996.
- (8) Greentree, A. D.; Aharonovich, I.; Castelletto, S.; Doherty, M. W.; McGuinness, L. P.; Simpson, D. A. 21st-Century applications of nanodiamonds. *Opt. Photonics News* **2010**, *21*, 20–25.
- (9) Aharonovich, I.; Greentree, A. D.; Praver, S. Diamond photonics. *Nat. Photonics* **2011**, *5*, 397–405.
- (10) Schirhagl, R.; Chang, K.; Loretz, M.; Degen, C. L. Nitrogen-vacancy centers in diamond: nanoscale sensors for physics and biology. *Annu. Rev. Phys. Chem.* **2014**, *65*, 83–105.
- (11) Gruber, A.; Drabentst, A.; Tietz, C.; Fleury, L.; Wrachtrup, J.; von Borczyskowski, C. Scanning confocal optical microscopy and magnetic resonance on single defect centers. *Science* **1997**, *276*, 2012–2014.
- (12) Jelezko, F.; Wrachtrup, J. Single defect centres in diamond: A review. *Phys. Status Solidi A* **2006**, *203*, 3207–3225.
- (13) Toyli, D. M.; de las Casas, C. F.; Christle, D. J.; Dobrovitski, V. V.; Awschalom, D. D. Fluorescence thermometry enhanced by the quantum coherence of single spins in diamond. *Proc. Natl. Acad. Sci. U.S.A.* **2013**, *110*, 8417–8421.
- (14) Acosta, V. M.; Bauch, E.; Ledbetter, M. P.; Waxman, A.; Bouchard, L. S.; Budker, D. Temperature dependence of the nitrogen-vacancy magnetic resonance in diamond. *Phys. Rev. Lett.* **2010**, *104*, 070801.
- (15) Toyli, D. M.; Christle, D. J.; Alkauskas, A.; Buckley, B. B.; Van de Walle, C. G.; Awschalom, D. D. Measurement and control of single nitrogen-vacancy center spins above 600 K. *Phys. Rev. X* **2012**, *2*, 031001.
- (16) Hui, Y.-Y.; Cheng, C.-L.; Chang, H.-C. Nanodiamonds for optical bioimaging. *J. Phys. D: Appl. Phys.* **2010**, *43*, 374021.
- (17) Mochalin, V. N.; Shenderova, O.; Ho, D.; Gogotsi, Y. The properties and applications of nanodiamonds. *Nat. Nanotechnol.* **2012**, *7*, 11–23.
- (18) Chang, Y.-R.; Lee, H.-Y.; Chen, K.; Chang, C.-C.; Tsai, D.-S.; Fu, C.-C.; Lim, T.-S.; Tzeng, Y.-K.; Fang, C.-Y.; Han, C.-C.; Chang, H.-C.; Fann, W. Mass production and dynamic imaging of fluorescent nanodiamonds. *Nat. Nanotechnol.* **2008**, *3*, 284–288.
- (19) Yu, Y.-Y.; Chang, S.-S.; Lee, C.-L.; Wang, C. R. C. Gold nanorods: Electrochemical synthesis and optical properties. *J. Phys. Chem. B* **1997**, *101*, 6661–6664.
- (20) Hui, Y.-Y.; Su, L.-J.; Chen, O. Y.; Chen, Y.-T.; Liu, T.-M.; Chang, H.-C. Wide-field imaging and flow cytometric analysis of cancer cells in blood by fluorescent nanodiamond labeling and time gating. *Sci. Rep.* **2014**, *4*, 5574.
- (21) Lai, N. D.; Zheng, D.; Treussart, F.; Roch, J.-F. Optical determination and magnetic manipulation of single nitrogen-vacancy color center in diamond nanocrystal. *Adv. Nat. Sci.: Nanosci. Nanotechnol.* **2010**, *1*, 015014.
- (22) McGuinness, L. P.; Yan, Y.; Stacey, A.; Simpson, D. A.; Hall, L. T.; Maclaurin, D.; Praver, S.; Mulvaney, P.; Wrachtrup, J.; Caruso, F.; Scholten, R. E.; Hollenberg, L. C. L. Quantum measurement and

orientation tracking of fluorescent nanodiamonds inside living cells. *Nat. Nanotechnol.* **2011**, *6*, 358–363.

(23) Chang, C.-K.; Wu, C.-C.; Wang, Y.-S.; Chang, H.-C. Selective extraction and enrichment of multi-phosphorylated peptides using polyarginine-coated diamond nanoparticles. *Anal. Chem.* **2008**, *80*, 3791–3797.

(24) Xu, C. S.; Cang, H.; Montiel, D.; Yang, H. Rapid and quantitative sizing of nanoparticles using three-dimensional single-particle tracking. *J. Phys. Chem. C* **2007**, *111*, 32–35.

(25) Carlson, M. T.; Green, A. J.; Richardson, H. H. Superheating water by CW excitation of gold nanodots. *Nano Lett.* **2012**, *12*, 1534–1537.

(26) Baffou, G.; Polleux, J.; Rigneault, H.; Monneret, S. Superheating and micro-bubble generation around plasmonic nanoparticles under cw illumination. *J. Phys. Chem. C* **2014**, *118*, 4890–4898.

(27) Chen, H.-J.; Shao, L.; Ming, T.; Sun, Z.-H.; Zhao, C.-M.; Yang, B.-C.; Wang, J.-F. Understanding the photothermal conversion efficiency of gold nanocrystals. *Small* **2010**, *6*, 2272–2280.

(28) Tzeng, Y.-K.; Faklaris, O.; Chang, B.-M.; Kuo, Y.; Hsu, J.-H.; Chang, H.-C. Superresolution imaging of albumin-conjugated fluorescent nanodiamonds in cells by stimulated emission depletion. *Angew. Chem., Int. Ed.* **2011**, *50*, 2262–2265.

(29) Geiselmann, M.; Marty, R.; García de Abajo, F. J.; Quidant, R. Fast optical modulation of the fluorescence from a single nitrogen–vacancy centre. *Nat. Phys.* **2013**, *9*, 785–789.

(30) Ekici, O.; Harrison, R. K.; Durr, N. J.; Eversole, D. S.; Lee, M.; Ben-Yakar, A. Thermal analysis of gold nanorods heated with femtosecond laser pulses. *J. Phys. D: Appl. Phys.* **2008**, *41*, 185501.

(31) Boulais, É.; Lachaine, R.; Meunier, M. Plasma mediated off-resonance plasmonic enhanced ultrafast laser-induced nanocavitation. *J. Phys. Chem. C* **2013**, *117*, 9386–9396.

(32) Richardson, H. H.; Carlson, M. T.; Tandler, P. J.; Hernandez, P.; Govorov, A. O. Experimental and theoretical studies of light-to-heat conversion and collective heating effects in metal nanoparticle solutions. *Nano Lett.* **2009**, *9*, 1139–1146.

(33) Ng, K. C.; Cheng, W.-L. Fine-tuning longitudinal plasmon resonances of nanorods by thermal reshaping in aqueous media. *Nanotechnology* **2012**, *23*, 105602.

(34) Ma, H.; Bendix, P. M.; Oddershede, L. B. Large-scale orientation dependent heating from a single irradiated gold nanorod. *Nano Lett.* **2012**, *12*, 3954–3960.

(35) Loza, P.; Kouznetsov, D.; Ortega, R. Temperature distribution in a uniform medium heated by linear absorption of a Gaussian light beam. *Appl. Opt.* **1994**, *33*, 3831–3836.

(36) Cordero, M. L.; Verneuil, E.; Gallaire, F.; Baroud, C. N. Time-resolved temperature rise in a thin liquid film due to laser absorption. *Phys. Rev. E* **2009**, *79*, 011201.

(37) Luo, T.-F.; Chen, G. Nanoscale heat transfer—from computation to experiment. *Phys. Chem. Chem. Phys.* **2013**, *15*, 3389–3412.

(38) Steinert, S.; Ziem, F.; Hall, L. T.; Zappe, A.; Schweikert, M.; Gotz, N.; Aird, A.; Balasubramanian, G.; Hollenberg, L.; Wrachtrup, J. Magnetic spin imaging under ambient conditions with sub-cellular resolution. *Nat. Commun.* **2013**, *4*, 1607.

(39) Cooper, A.; Magesan, E.; Yum, H. N.; Cappellaro, P. Time-resolved magnetic sensing with electronic spins in diamond. *Nat. Commun.* **2014**, *5*, 3141.

(40) Matsuo, S.; Misawa, H. Direct measurement of laser power through a high numerical aperture oil immersion objective lens using a solid immersion lens. *Rev. Sci. Instrum.* **2002**, *73*, 2011.